Effects of Aft Angle on Non-equilibrium Flows over Double Cone at High Enthalpy

First A. Dengke Li[1], Second B. Bo Sun[2], Third C. Chunliang Dai[3], Fourth D. Xiong Chen[4]

Abstract

To understand the effects caused by the different aft angles on non-equilibrium flows over double cone, high enthalpy (21.77MJ/kg) flows over double cones with aft angles of 45°,50°,55° and 60° are numerically investigated in the present work. Considering the non-equilibrium effects, the Naiver-Stokes equations coupled with two- temperature model and a seven-species chemical kinetic model are employed to simulate the flow. The enhanced aft angle and the change in shock structures lead to a higher adverse pressure gradient at the vicinity of compressed corner, such that the separation zone extends along both upstream and downstream. In flows of double cone with 45° and 50° aft angle, the shock-shock interactions are close to the Edney type-VI interaction. Whereas, Edney type-IV interaction and secondary separation vortex appear in flow fields of double cone with 55° and 60° aft angle. The strong reaction and thermo non-equilibrium primarily occur just downstream the second cone shock. When aft angle below 55°, the increasing aft angle deepens the degrees of nitrogen dissociation, nitric oxide ionization and thermo non-equilibrium. When aft angle beyond 55°, since the intensity of the strongest part of second cone shock remains unchanged with the increasing aft angle, the degrees of those processes are not sensitive to the aft angle. The increase of aft angle changes the distribution of wall parameters, which are evidenced by a higher maximum wall pressure and wall heat flux in the vicinity of the compressed corner. Overall, the significant differences of flow characteristics are between the flows of 50° and 55° configuration, causing by the transition of shock-shock interaction type.

Keywords: High enthalpy, Aft angle, Non-equilibrium effects, Separation zone, Shock-shock interaction

Nomenclature

Latin
D -- Diffusion coefficient
E – Total energy per unit mass
H – Total enthalpy per unit mass
L – Length of cone
T – Temperature
Y – Mass fraction
n – Total number of species
p – Pressure

t – Time
u – Velocity
Greek
θ – Cone angle
ρ – Density
τ – Stress tensor
ω – Source term
Subscripts

[1] *Nanjing University of Science and Technology, No. 200 Xiaolingwei Street, Nanjing, Jiangsu Province, China, 15651761651@163.com*

[2] *Nanjing University of Science and Technology, No. 200 Xiaolingwei Street, Nanjing, Jiangsu Province, China, hypersun@126.com*

[3] *Nanjing University of Science and Technology, No. 200 Xiaolingwei Street, Nanjing, Jiangsu Province, China, DCL3839@126.com*

[4] *Nanjing University of Science and Technology, No. 200 Xiaolingwei Street, Nanjing, Jiangsu Province, China, chenxiong@njust.edu.cn*

i, j, k – Directions

tr – Translational-rotational

ve – Vibrational-electronic

s – Species of mixture

1. Introduction

Shock-shock interaction (SSI) and shock wave-boundary layer interaction (SWBLI) are common phenomenon in the flows of hypersonic aircraft [1,2], which can lead to excessive heat transfer and pressure loads on aircraft surfaces, posing a risk of damage to the aircraft structure in hypersonic flow [3,4]. Hypersonic vehicles often exhibit geometry configurations that inherently give rise to SWI and SWBLI phenomena, such as double cones, double wedges, cylinder flares, and compressed corners. Therefore, it becomes imperative to investigate the flow characteristics of SWBLI and SWI, as such insights can significantly contribute to the development of hypersonic vehicle designs.

A number of experiments were conducted in wind tunnels to study the hypersonic flow over double cones and double wedges in previous [5-10]. Since wind tunnel tests are resource intensive and difficult to reproduce, many studies have been conducted numerically based on flow conditions from wind tunnels. There have been a number of studies focusing on the comparison of experimental and numerical results [11-16]. The numerical results exhibited satisfactory agreement with the experimental data obtained in low to moderate enthalpy conditions. While significant discrepancies were observed for the experiments at high enthalpies, since the thermochemical non-equilibrium effects were evident [17]. Up to now, the reasons for the discrepancies are still not fully explained, a further investigation of high enthalpy double cone/wedge flow is needed to better understand the underlying mechanism. In addition, the thermochemical non-equilibrium effect is a hot topic of research focus on flow over a double cone/wedge at high freestream enthalpy [18-22]. Kianvashrad et al. [18] and Dai et al. [22] both found that the non-equilibrium models predict smaller separation zones and lower heat flux than the thermal perfect gas model.

In investigations aforementioned, most of the geometries were fixed to better compare the differences caused by the thermochemical non-equilibrium effect or reproduce the experiment result. Nevertheless, the geometry configurations of different hypersonic vehicles in practical applications are variable. Thus, there are also several studies that pay attention to the effects of the geometric change in hypervelocity flows over a double cone/wedge. Durna et al. [23] numerically investigated the shock interaction mechanisms on double wedges at Mach 7. The aft angles were set as 30° and 45°–60°. The flow was assumed nonreaction considering the low freestream enthalpy. With an increasing aft angle, they found that the positions of the heat transfer peak moved towards the compressed corner. On the other hand, they observed a two-way-coupled unsteady mechanisms between the second cone shock and boundary layer. The existence of a critical value of aft angle which determines the occurrence of the two-way coupled mechanisms was proved in this study. The exact angular thresholds were then derived in their later study [24]. Their results showed that flow with periodic behaviors occurs when the aft angle exceeds 47°. Celik et al. [25] broadened the study to high enthalpy flows in 2021. They found that the affected areas of reactions expand with the aft angle increasing and reactions start to take place in the separation zone when aft angle is beyond 55°. Meanwhile, the significant increase in the rate of chemical reactions can also be concluded. When the value of aft angle increased, the fluctuation magnitudes and time-averaged values of wall heat transfer and pressure in high enthalpy flows are larger than the lower ones, which represents more intense SSI and SWBLI. Hao et al. [26] numerically investigated the effect of leading-edge bluntness on hypersonic flows over double cone. The results showed that a small bluntness has few effects on the separation bubble sizes, shock wave structures, distributions of wall heat flux, and wall pressure. But the separation zone will expand dramatically when the blunt radius beyond a critical value.

Above all, the previous studies revealed that the geometric changes of double cones/wedges have evident influences on the flow characteristics. However, the total enthalpy in the previous studies that focus on the effects of the geometric changes of double cone/wedge flows are relatively low (below 13MJ/kg). For higher enthalpy flow over a double cone, the thermochemical non-equilibrium effects on flow are more pronounced and the flow characteristics are different. Under such conditions, the effect of aft angle variation on the flow is not clear. However, these effects and the underlying mechanisms behind them can be guidance for the design of hypersonic vehicles. Therefore, there is a need for corresponding researches of this issue. The objective of the present study is to understand the effects caused by the aft angle variation in high enthalpy flow over double cones. The full text is organized as

follows: Firstly, the sets of geometry and flow are introduced. Secondly, the governing equation and numerical method are given, and the numerical method is validated. Finally, the flow field structure, thermochemical non-equilibrium effect and wall parameters of the four configurations are compared and analyzed.

2. Geometric configuration and flow conditions

The basic model of double cone in present study is from the experiment conducted in the Large Energy National Shock Tunnel (LENS-XX) at the Calspan-University at Buffalo Research Center (CUBRC) in 2013 [5]. Six separate runs were performed in this experiment, the total enthalpies of the freestream were set between 5.44-21.77MJ/kg and the Mach numbers were set between 10.90-13.23. The model of a double cone is depicted in Fig.1, its fore angle θ_1 is 25°. The first cone length L_1, second cone length L_2 and cylinder length L_3 are 106 mm, 107.4 mm and 40 mm, respectively. To obtain the effect of the various aft angles, the aft angle θ_2 is varied between 45°-60° at intervals of 5 degrees while the fore angle and the length of each cone are fixed.

The freestream condition used in the present work is from the run 4, which enthalpy is the highest all over the six runs. The freestream is considered a thermochemical equilibrium air mixture that only include nitrogen molecules and oxygen molecules with the mass fraction of 0.765 and 0.235, respectively. The flow can be assumed as a fully laminar flow because of the low Reynolds number. The freestream conditions of run 4 are depicted in Table 1.

(a) The geometry configuration.   (b) Computational domain
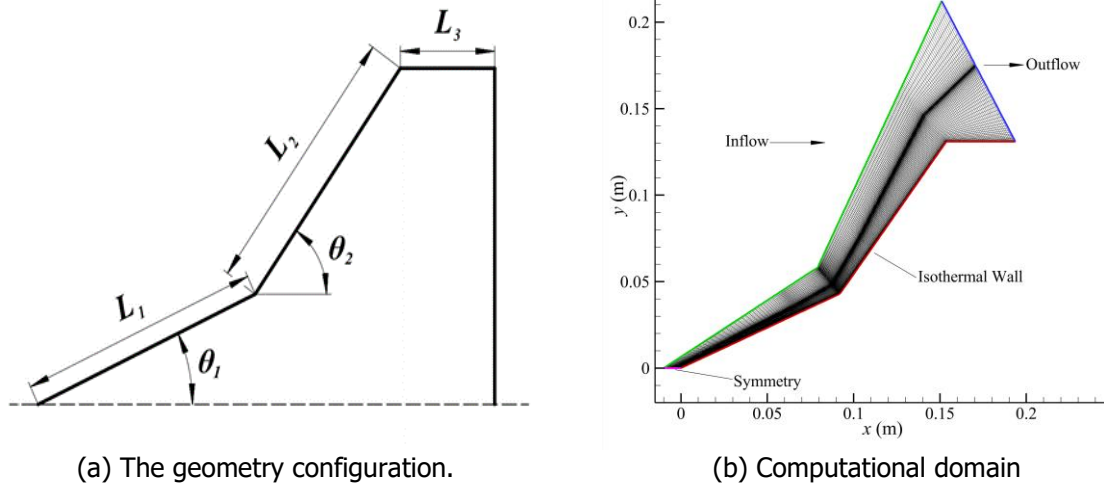
Fig 1. The geometry configuration and computational domain of the double cone.

Table 1. Free stream conditions.

Total Enthalpy (MJ/kg)	Mach number	Velocity (m/s)	Density (kg/m3)	Static temperature (K)
21.77	12.82	6497	0.000964	652

3. Methods and validation

3.1. Governing equations and physical models

The multi-species Naiver–Stokes equations coupled with two-temperature model are employed to model the high enthalpy flows in present study, involving conservation equations of mass, momentum, total energy and vibrational energy:

$$\frac{\partial \rho_s}{\partial t} + \frac{\partial \rho_s u_i}{\partial x_i} = \frac{\partial}{\partial x_i}(\rho D_s \frac{\partial Y_s}{\partial x_i}) + \omega_s \tag{1}$$

$$\frac{\partial \rho u_i}{\partial t} + \frac{\partial \rho u_i u_j}{\partial x_j} = -\frac{\partial p}{\partial x_i} + \frac{\partial \tau_{ij}}{\partial x_j} \tag{2}$$

$$\frac{\partial \rho E}{\partial t} + \frac{\partial \rho H u_i}{\partial x_i} = \frac{\partial}{\partial x_i}\left(u_i \tau_{ij} + q_{tr,i} + q_{ve,i} + \sum_{s=1}^{ns} \rho D_s H_s \frac{\partial Y_s}{\partial x_i}\right) \tag{3}$$

$$\frac{\partial \rho e_{ve}}{\partial t} + \frac{\partial \rho e_{ve} u_i}{\partial x_i} = \frac{\partial}{\partial x_i}\left(q_{ve,i} + \sum_{s=1}^{ns} \rho D_s e_{ve,s} \frac{\partial Y_s}{\partial x_i}\right) + \omega_{ve} \tag{4}$$

where ρ_s, D_s, Y_s and ω_s are the density, diffusion coefficient, mass fraction, and mass generation rate of species s, respectively; u_i and u_j are the velocity of the i and j directions, respectively; p and ρ are the density and pressure of the species mixture, respectively. And τ_{ij} is the shear stress tensor based on Newtonian fluid with Stokes' hypothesis. In equation (3), E and H are the specific total energy and total enthalpy, respectively; $q_{tr,i}$ and $q_{ve,i}$ are the translational-rotational heat transfer and vibrational-electronic heat transfer in i direction, respectively. In equation (4), e_{ve} and ω_{ev} are the vibrational-electronic energy and vibrational source term, respectively.

The two temperature model established by Park [27] is used to model the thermal non-equilibrium process. The vibrational relaxation time is obtained by using Millikan-White equation with high temperature corrections [28]. The reactions in air are modeled by a chemical kinetic model including seven species (N_2, N, O_2, O, NO, NO^+, e^-) and six reactions [22]. The forward reaction rates are calculated by Arrhenius equation and the backward reaction rates are obtained from equilibrium constant. Then the vibrational source term can be calculated as:

$$\omega_{ve} = e_{v-t} + \sum_{s=1}^{n} \omega_s e_{ve,s} \tag{5}$$

where the first term at right side represents the energy exchange between translational-rotational mode and vibrational-electronic mode and can be obtained by applying Landau-Teller model [29]. While the second term represents the vibrational-electronic energy change caused by chemical reactions.
The individual species' viscosities and thermal conductivities are calculated by applying Gupta's [30] viscosity curve fits. Then these properties of mixture are obtained by Wilke's Law [31]. The modified Fick's law is used to obtain the species mass diffusion fluxes, ensuring their collective sum remains zero [32]. A constant Schmidt number of 0.525 is used to calculate the diffusion coefficient.

3.2. Numerical method and boundary conditions

A 2-D multiblock structured mesh is generated to ensure good mesh qualities and save computational resources. The computational domain is shown in Fig.1 (b). The cone surfaces are set as no-slip wall with a constant temperature of 300 K. The catalytic effects on surfaces are not considered. The flow field is initialized with the parameters of the freestream. The vibrational–electronic temperature and translational-rotational temperature are taken the same value at the inflow boundary.

Finite volume method is employed to solve the Naiver–Stokes equations. The flux of the inviscid term is calculated by an approximate Riemann solver named Harten-Lax-van Leer Contact (HLLC) [33]. A second order total variation diminishing (TVD) scheme [34] that can avoid introducing new maxima and minima in the reconstruction is used to reconstruct the values of the cell centers. A fully implicit scheme is used to discrete time term. We considered the convergence is achieved when the flow structure remains unchanged and the residuals below 10^{-3}.

(a) Comparison of wall heat flux (b) Comparison of wall pressure
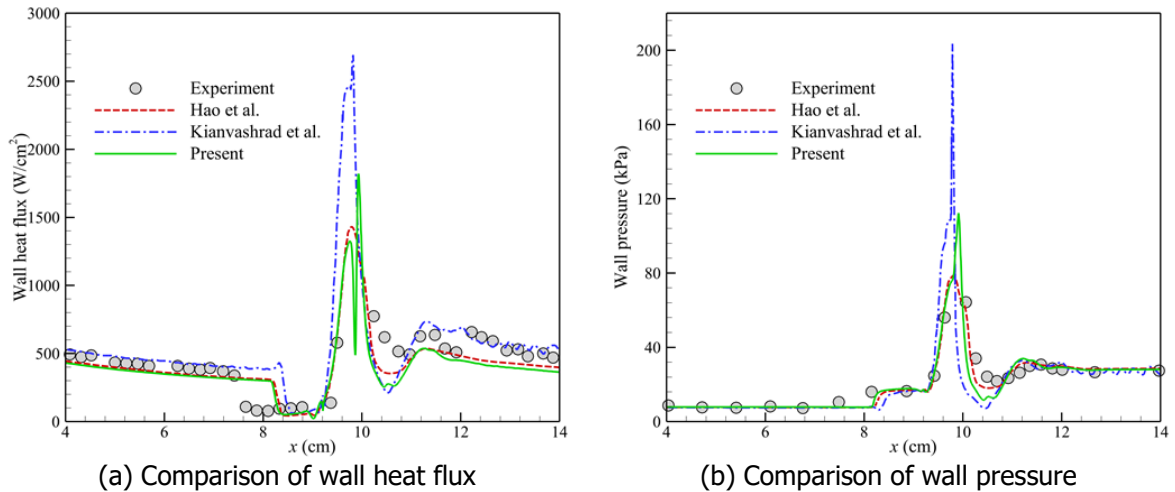
Fig 2. Comparison of wall parameters with reference data.

3.3. Method validation and grid convergence study

Fig.2 illustrates the wall parameters (heat flux and wall pressure) of present study and the experimental results [5], numerical results of Hao et al. [16], and Kianvashrad et al. [18]. The peak values of wall heat flux and wall pressure calculated by the present method are between the peak values of Hao et al. and Kianvashrad et al. The two peaks of wall heat flux around the reattachment point and impingement point can be clearly distinguished by present method. But there is only one wall heat flux peak can be seen in the results calculated by Hao et al. The cause of the above difference is that the reattachment point calculated by Hao et al. is very close to the impingement point of shock. Such that there is only one peak of heat flux can be observed. The position of the peaks in present study is little closer to the downstream than the others. Regrettably, sensor distribution near the corner of cones is not dense enough to capture all flow field characteristics. At the moment, it can only say that all three numerical results are broadly reasonable. In other aspects, the separation point calculated in present study is the most consistent with the experiment results. The wall heat flux obtained by Kianvashrad et al. is the closest to the experiment results on the downstream of second cone, while the results of Hao et al. and present study are lower than the experiment results. To sum up, although the results in present study have a few disparities with the references, it can say that the differences between the present results and references are within the allowable error range.

(a) Wal heat flux. (b) Wall static pressure
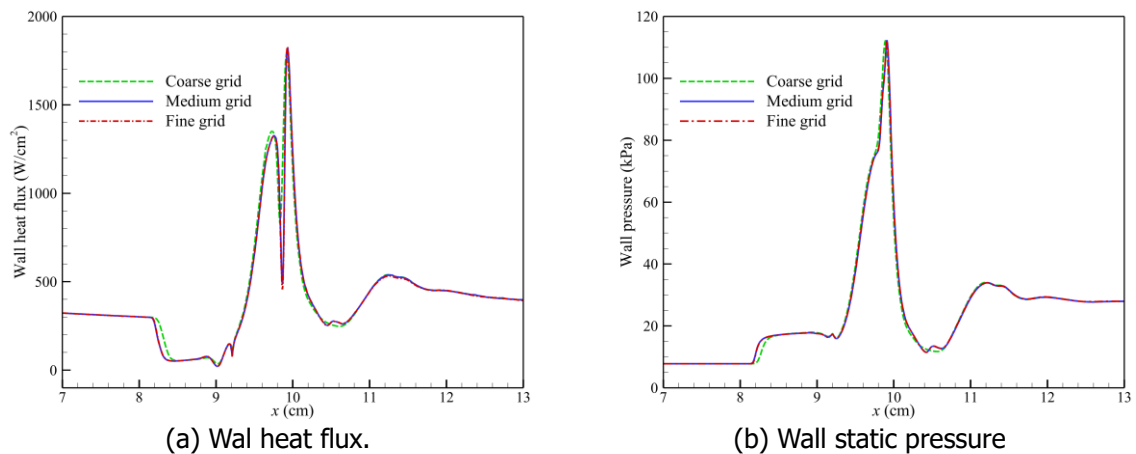
Fig 3. Wall parameters of different grids.

To verify the grid convergence, the coarse, medium and fine grids are employed with the cells number of 200×600,400×1200 and 600×1800, respectively. To better capture the flow features, the grids near the shock wave and boundary layer have been properly encrypted. To maintain the cell Reynolds number below 1, the normal height of the first layer of mesh is set to 1×10^{-7} m. The wall heat flux and static pressure predicted by the different grids are shown in Fig.3. The coarse grids underestimate the

separation zone length. On the other hand, the wall parameters distribution calculated by the medium and fine grid are almost the same. So, the medium grid is used in present study.

4. Results and discussion
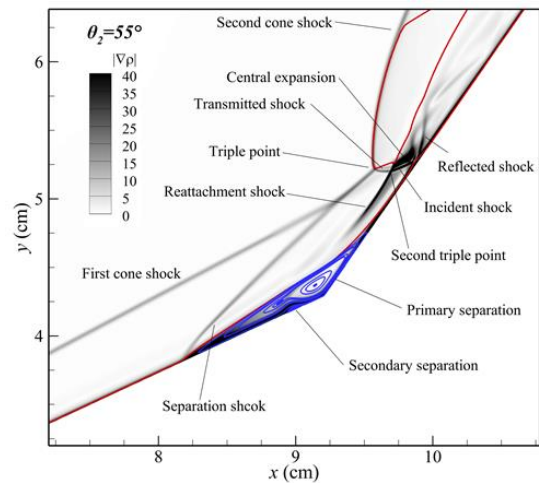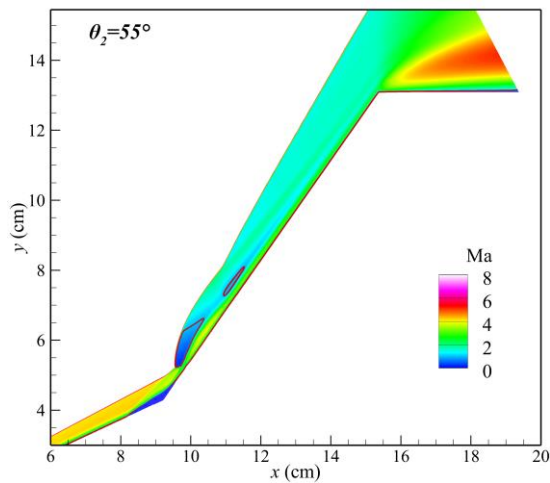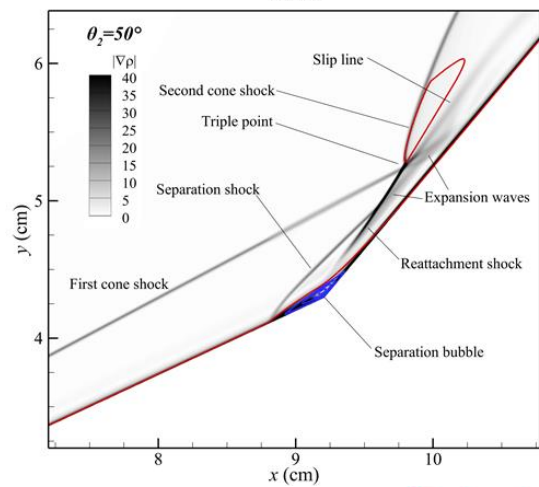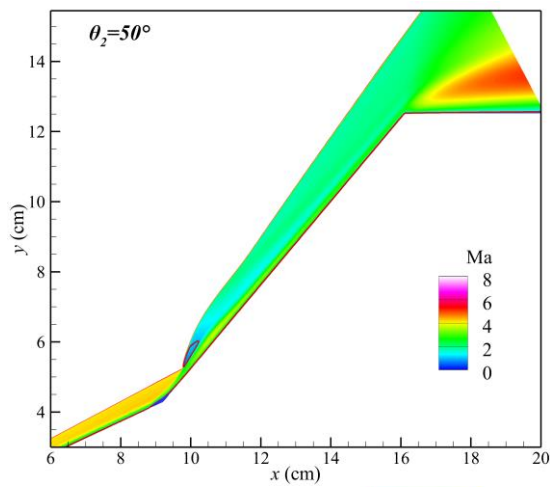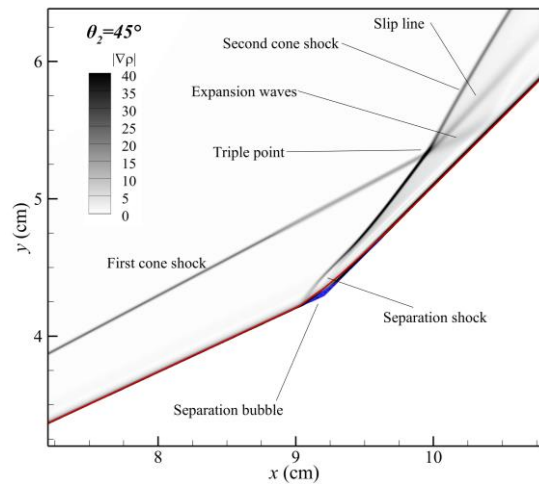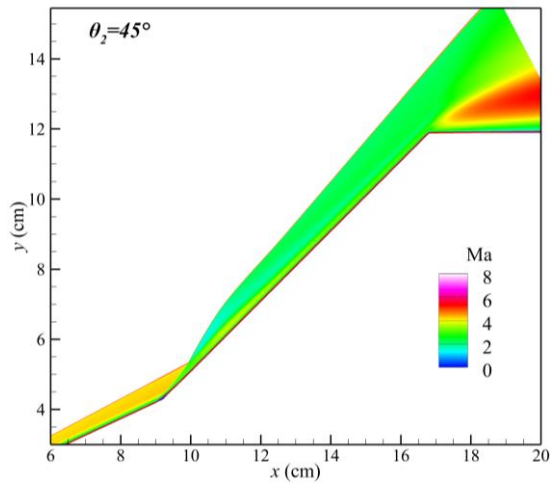
4.1. Analysis of the shock wave structure

The contours of Mach number and density gradient in the flow fields of different configurations are shown in Fig.4, the red lines and dark blue lines represent the sonic line and streamlines, respectively. It can be clearly found that the shock structures change significantly with the increase of aft angle. For the case of 45° configuration, the inverse pressure gradient at the compressed corner induces the flow separation. Due to the small separation zone, the progressively darker separation shock in the density gradient contour means that the separation shock immediately interacts with the compressed waves caused by reattachment and is reinforced. The separation shock interacts with the first cone shock at the triple point, followed by the formation of the second cone shock, a slip line, and expansion waves. The above features suggest that the shock wave structure belongs to Edney type-VI SSI [35]. In the contours of Mach number, after the higher intensity part of the second cone shock, a low Mach number band area along the flow direction is formed. As the second cone shock gradually deflects to the cone, the shock intensity rapidly weakens.

The shock wave structure in the flow field of 50° configuration is similar to that of the 45° configuration, but shock wave interactions is stronger. As a result, a curved second cone shock is formed after the triple point and a small subsonic region appears after the second cone shock. As described by Olejniczak et al. [7], this shock interaction can be identified as a supercritical type VI SSI. In addition, the expansion of separation zone can be seen clearly in the contours of density gradient. Hence, separation shock is generated at the position closer to the upstream, causing the triple point move upstream.

Compared to the configuration with smaller aft angles, more complex shock wave structures appear in the flow field of 55° configuration. Due to the extension of separation zone, the separation shock no longer interacts with the reattachment shock but interacts with the first cone shock and deflected downward. Then it interacts with second cone shock at the triple point, followed by the formation of a transmitted shock and a supersonic jet wrapped between the contact surface and boundary layer. The above features indicate that the shock wave structure can be classified as Edney type-V SSI [35]. The transmitted shock interacts with the reattachment shock at second triple point and forms an incident shock. The incident shock impinges on the second cone producing a reflected shock. The reflected shock continuously reflecting between the contact surface and the second cone. In order to maintain the continuity of pressure, the reattachment shock striking the contact surface must form a central expansion to offset the pressure rise over the reattachment shock, which is then reflected in the boundary layer as a compression wave. Next, the compression wave reflects in the contact surface and forms expansion waves. This cycle of reflections of compression waves and expansion waves continues [36]. On the other hand, the action of shocks and expansion waves leads to an uneven contact surface. The second cone shock has a higher strength and standoff distance than the one of configuration with a smaller aft angle, causing the subsonic region extend downstream and become thicker. At the area more downstream, compression waves at the contraction position of the supersonic jet forming another small subsonic region. Another notable feature is the appearance of secondary separation vortices. The formation of secondary separation vortices is mainly caused by the inverse pressure gradient that forms in the reattachment region encountered in the development of the reverse flow boundary layer.

As the aft angle increases to 60°, the further increase in standoff distance, curvature and strength of the second cone shock can be observed. In the contour of Mach number, there are two subsonic regions after the second cone shock. The formation of the larger one has been interpreted in the previous paragraph. The formation of the smaller one is mainly due to the more intense compression waves caused by the more rapidly contraction of the supersonic jet. The compression waves enhance the strength of the original weaker region of the second cone shock, making the second cone shock convex again. Another low Mach number band area along the flow direction forms after this convex part of second cone shock. The further extension of the separation zone makes the triple point locate further away from the cone surface, so the transmitted shock becomes longer. In addition, the reattachment of the shear layer is not finished before the impingement point of incident shock, which is difficult to find in the contour of density gradient and will be discussed in Sec 4.3.
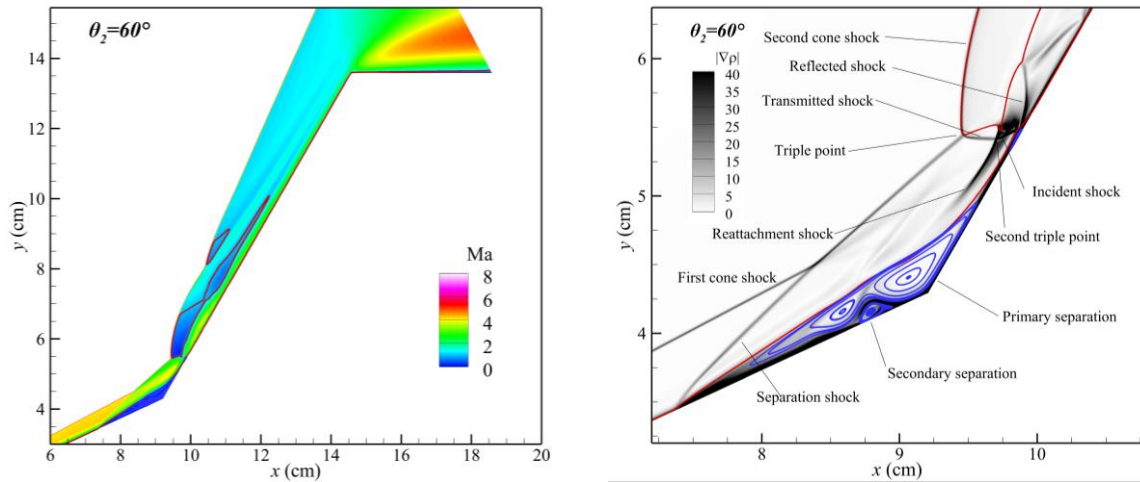
Fig 4. The shock structures of double cones with different aft angle.

4.2. Analysis of thermochemical non-equilibrium process

Fig.5 shows the contours of translational-rotational temperature and the difference between translational-rotational temperature and vibrational-electronic temperature (ΔT) in the flows of different aft angle configurations. The black lines represent the contour line of ΔT equal to zero. In the every flow field, there is a high-temperature zone of translational-rotational temperature just behind the second cone shock. Downstream of the high temperature zone, the translational-rotational temperature gradually decreases. This is due to the fact that the flow through the shock is close to thermochemical freezing state, the kinetic energy of the freestream is mainly transformed into translational-rotational energy. This process leads to a steep increase of the translational-rotational temperature. Subsequently, the gas molecules begin to dissociate while the vibrational energy is excited, the vibrational-electronic temperature increases and the translational-rotational temperature gradually decreases.

Compare the four flow fields, there are mainly two effects in thermo non-equilibrium process caused by the increasing aft angel. Firstly, the larger the aft angle, the higher the translational-rotational temperature and ΔT in the region just behind the second cone shock. The differences in maximum values of translational-rotational temperature and ΔT between the flow of the 45° configuration and the 60° configuration are both over 3000 K. This because the second cone shock in flow flied with a larger aft angle is stronger, resulting in a higher post-shock temperature and a higher degree of thermo non-equilibrium. In addition, the relative difference in the peak value of ΔT and translational-rotational temperature is quite small between 55° and 60° configuration, being 0.74 % and 1.29 %, respectively. This is because the strongest parts of the two second cone shock are both very close to a normal shock. Secondly, in the flow of 55° and 60° configuration, there are regions with negative ΔT in supersonic jet and separation zone. This is called vibration overexcitation phenomenon [37]. After the expansion waves in supersonic jet, the translational- rotational energy drops quickly while the vibrational energy decreases slowly, since the relaxation time is quite long when the local translational-rotational temperature and static pressure is low. As a result, the non-equilibrium in the two-energy mode manifests a negative ΔT. The mechanism of the vibration overexcitation phenomenon in separation zone is similar. In the flow of 45° and 50°configuration, the ΔT is always positive in the shock layer, meaning the thermo status is always non-equilibrium.
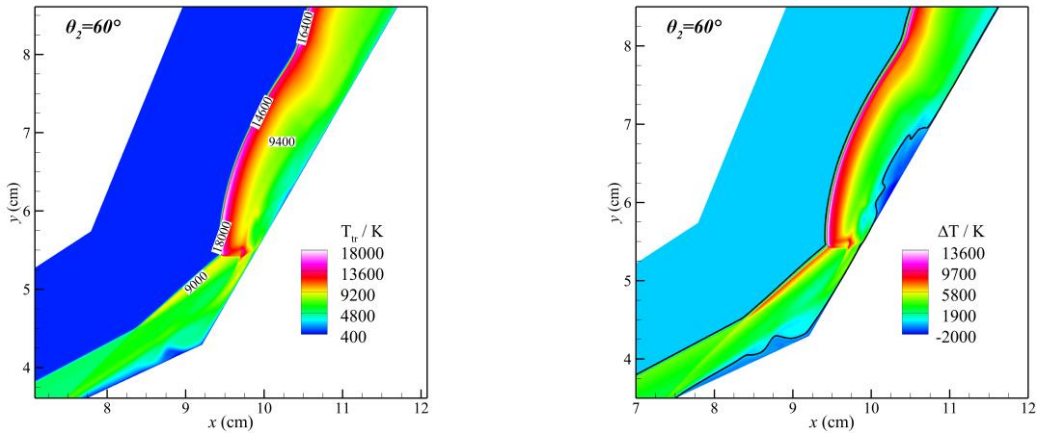
Fig. 6 shows the mass fraction of nitrogen and nitric oxide ion in the flow over different configurations. In each flow field, the dissociation reaction of nitrogen molecule mainly occurs downstream of the second cone shock. The minimum mass fraction of nitrogen molecule in the four flow fields are 0.661, 0.612, 0.565 and 0.557, respectively. The maximum mass fraction of nitric oxide ion in the four flow fields are 0.00047, 0.00096, 0.0013 and 0.0013, respectively. Those indicate that the degree of nitrogen dissociation and the ionization of nitric oxide become deeper as the aft angle increases. But when aft angle beyond 55°, the degree of nitrogen dissociation and the ionization of nitric oxide are not sensitive to the aft angle. The main reason can be explained as follows: The minimum mass fraction of nitrogen
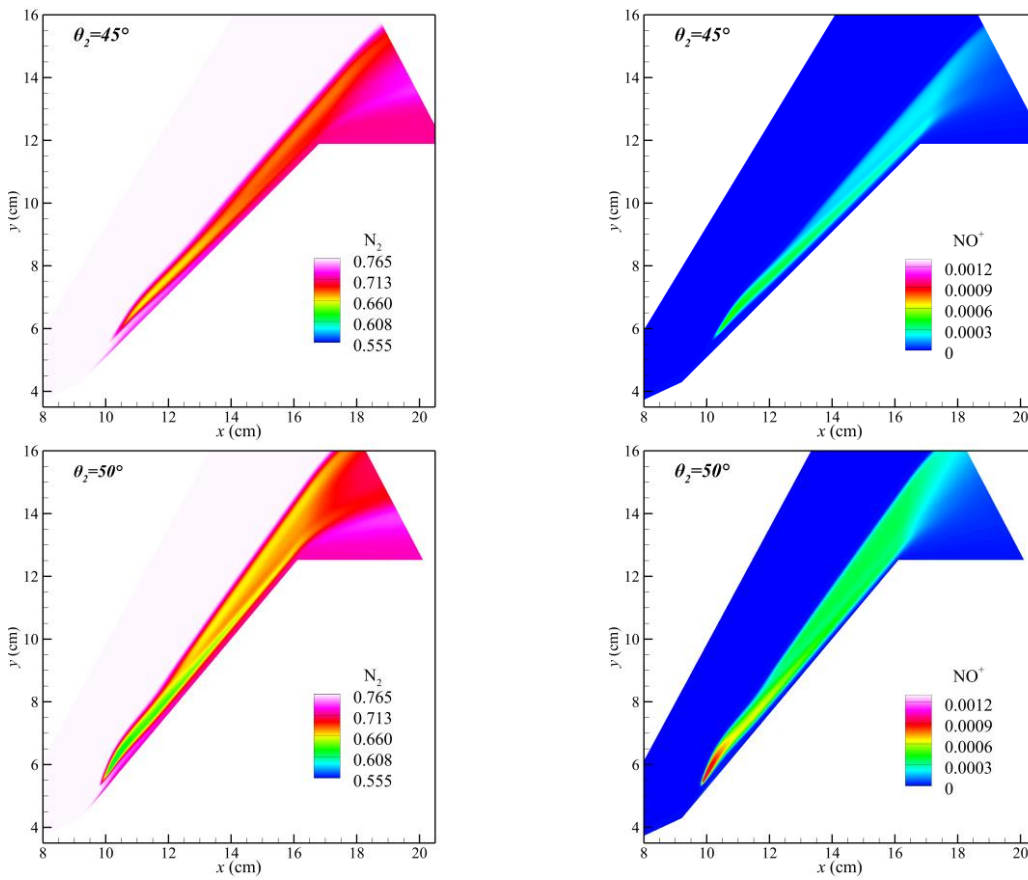
and the maximum mass fraction of nitric oxide ion are located downstream of the strongest part of the second cone shock. Since the temperature after the strongest part of the second cone shock is the highest. The strongest part of the second cone shock is very close to a normal shock when aft angle beyond 55°, so the post shock temperature remains the same value as the aft angle increase.

For the 45° and 50° configuration, the flow over the first cone is chemically frozen while the dissociation reaction of nitrogen takes place in the separation zone in the flow of the 55° and 60° configurations. Since the separation zones the flow of the 55° and 60° configurations are much larger than those in the flow of 45° and 50° configuration, the local flow characteristic time is longer. In addition, the mass fraction of nitrogen in downstream zone of the expansion corner decreases as the aft angle increases.
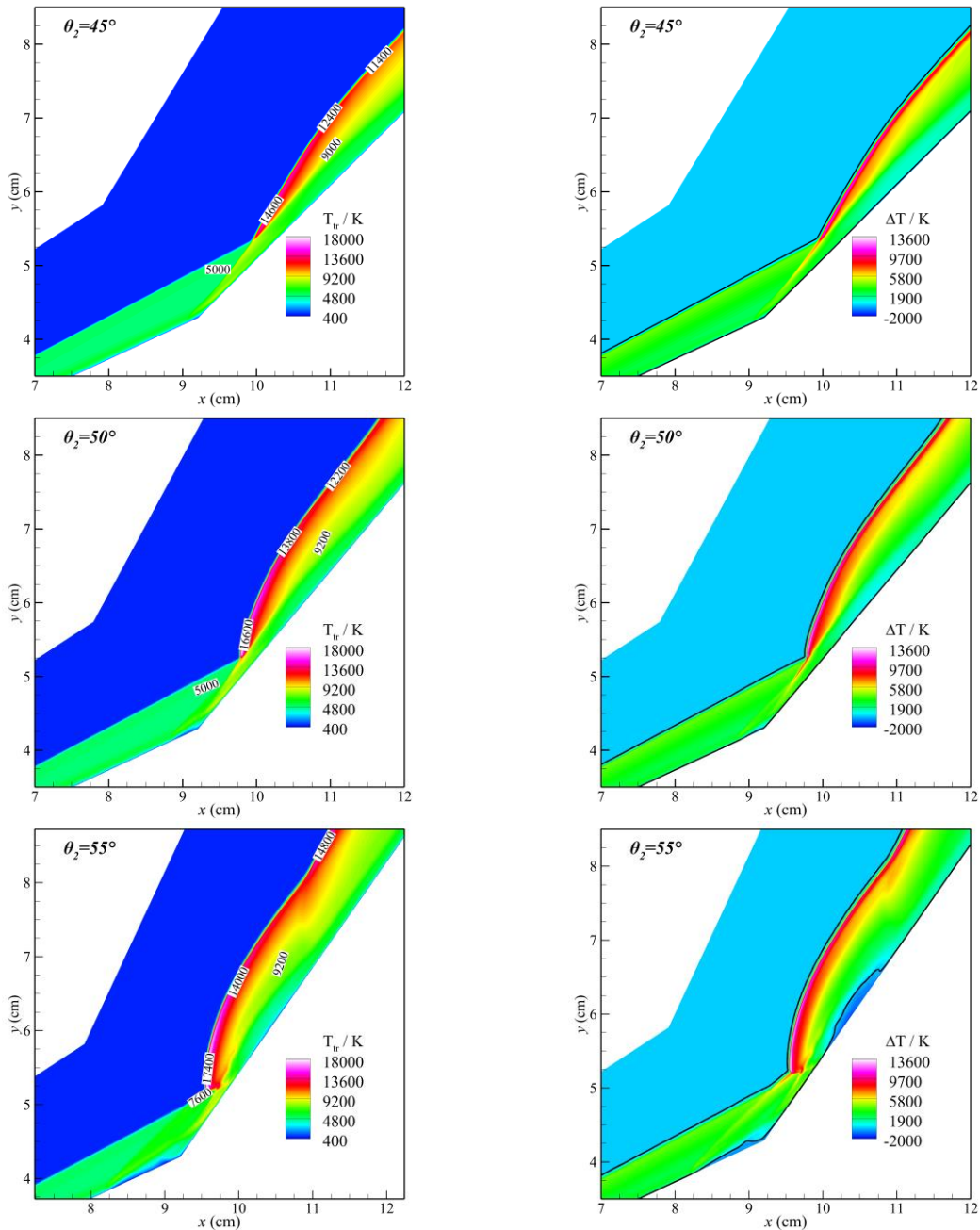
Fig 5. The distribution of T_{tr} and ΔT of double cones with different aft angle.

Dengke Li. First, Bo Sun. Second, Chunliang Dai.Third, Xiong Chen.Fourth
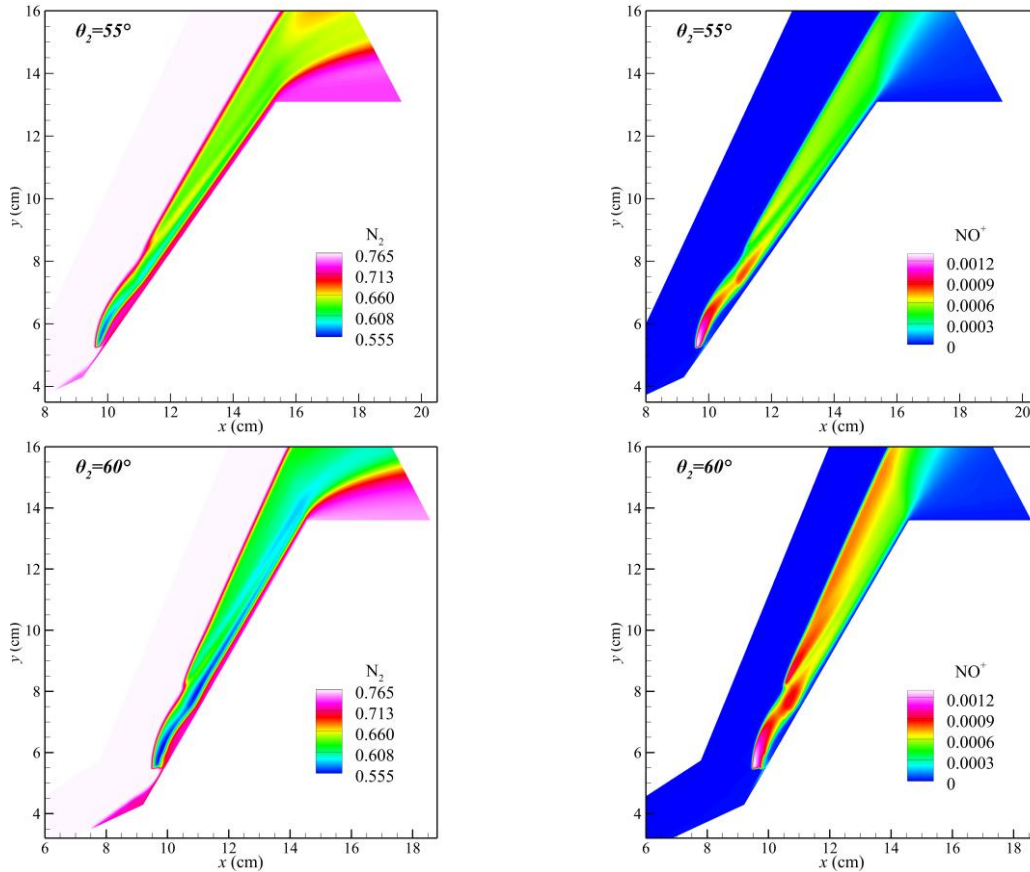
Fig 6. The mass fraction of nitrogen and nitric oxide ion in flow with different aft angle.

4.3. Analysis of the wall parameters

The distribution of skin friction coefficient along the surface is shown in Fig.7, the zero line of skin friction coefficient is indicated in dashes. As aft angle increases from 45° to 60°, the separation onset points are located at 10.04 cm, 9.76 cm, 9.06 cm and 8.18 cm away from the conical point, respectively. The reattachment points are located at 10.31 cm, 10.50 cm, 10.8 cm and 11.56 cm away from the conical point, respectively. During the three increases of the aft angle, the separation length expands by 174%, 135% and 94% than the previous one, respectively. This indicates that the influence of the enhanced aft angle on the separation length becomes weaker. For the 55° configuration, the impingement of incident shock induces one more separation at 11.3 cm from the conical point. However, the separation is so tiny that it can hardly be observed from the contour of density gradient. For 60° configuration, the skin friction coefficient gradually increases in the area between 10.85 cm and 11.25 cm away from the conical point while when it is close to zero it starts to drop down. This suggests that during the process of flow reattachment, the inverse pressure gradient caused by incident shock downstream turns the boundary layer develop towards the trend of separation again, delaying the emergence of the reattachment point. As shown in Fig.7(b), there are at least two minima $\tau_{1,min}$ and $\tau_{2,min}$ in the separation zone of every flow field except 45° configuration. Tang et al. [38] believes that the two minima are mainly resulting from the inverse pressure gradient caused by the separation shock and reattachment shock, respectively. And the presence of second minima is one of the characteristic features of a large separation zone [39]. Because of the onset of the secondary separation vortexes, several minima and maximum points can be observed at the vicinity of the compressed corner of the 55° and 60° configuration. For the 60° configuration, the inverse pressure gradient induced by incident shock leads to another minima in separation zone.
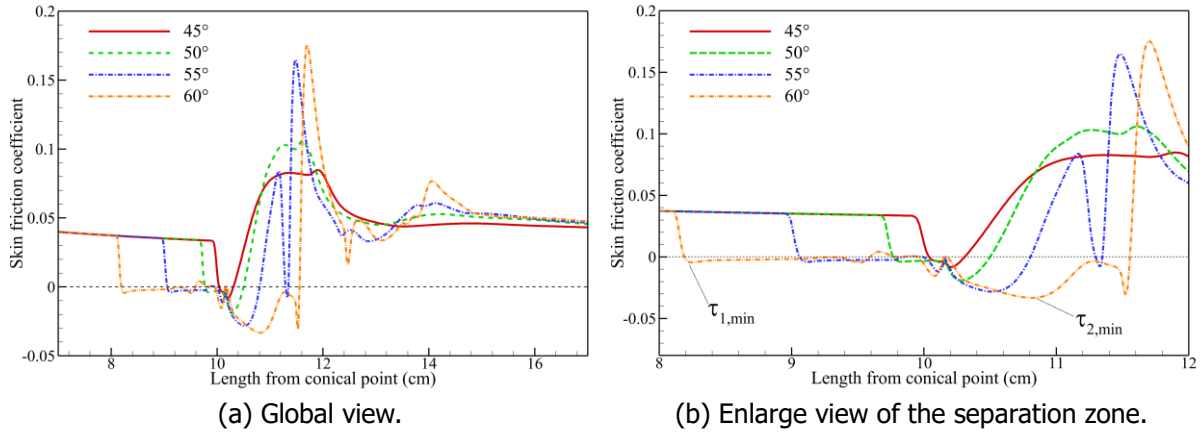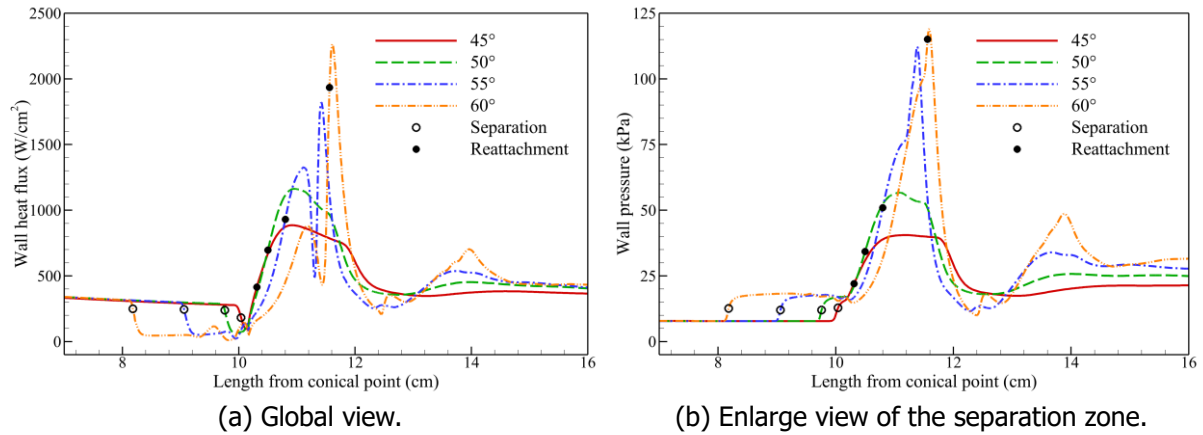
(a) Global view. (b) Enlarge view of the separation zone.

Fig 7. Distribution of skin friction coefficient.

(a) Global view. (b) Enlarge view of the separation zone.

Fig 8. Distribution of wall pressure and wall heat flux.

Fig.8 shows the distribution of wall heat flux and wall static pressure for different configurations. As aft angle increases from 45° to 60°, the maximum values of wall heat flux are 885 W/cm^2, 1162 W/cm^2, 1820 W/cm^2 and 2259 W/cm^2, respectively. And the maximum values of wall pressure are 40 kPa, 56 kPa, 111 kPa and 119 kPa, respectively. This indicates that the maximum values of wall heat flux and wall pressure increase as the aft angle increases. The largest difference of the maximum wall heat flux and wall pressure are between 50° configuration and 55° configuration, with 57 % and 98 %, respectively. This significant increase is mainly due to the different intensity of SSI and SWBLI in the different configurations. In the flow of 45° configuration and 50° configuration, the maximum values of wall heat flux and wall pressure are caused by the flow reattachment. There is only one peak located at the compressed corner.

However, the SSI and SWBLI in flows of the other two configurations are quite stronger, resulting in different distribution of wall heat flux and wall pressure. There are two peaks of wall heat flux located at the vicinity of the compressed corner, while there is only one peak of wall pressure. The lower peak of the wall heat flux is induced by the flow reattachment. The higher peak is induced by the impingement of the incident shock. The formation of the peak of wall pressure can be mainly divided into two stages. The first stage is started from the end of the pressure plateau, which is caused by the flow reattachment. The second stage is started from the point located just upstream to the peak point, which is caused by the impingement of the incident shock. For 60° configuration, there is a third peak value located 14 cm away from the conical point. It is related to the rapid contraction of the supersonic jet.

Besides affecting the peak value, increasing the aft angle also leads to the following effects on wall parameters. Firstly, fluctuations of wall parameters can be found after the second peak value drop-down in the flows of 55° configuration and 60° configuration, especially for the 60° configuration. These fluctuations are caused by the shock waves and expansion waves in the supersonic jet. Secondly, several fluctuations of wall heat flux can be seen in the separation zone due to the presence of

Dengke Li. First, Bo Sun. Second, Chunliang Dai.Third, Xiong Chen.Fourth

secondary separation vortices in the flows of 55° configuration and 60° configuration. Thirdly, with the expansion of the separation zone, the region of lower wall heat flux extends. The locations of the maximum wall heat flux and wall pressure move closer to downstream.

5. Conclusions

The high enthalpy flows over double cone with aft angles from 45° to 60° are numerical investigated by applying a thermochemical non-equilibrium gas model. The effects of increasing the aft angle on the flow characteristics are analyzed.

As the aft angle increases, the intensity of shock interactions, the standoff distance of second cone shock and the separation size increase. When aft angle increases from 50° to 55°, the SSI converts from Edney type-VI interaction to Edney type-V interaction while secondary separation vortex appears.

As the aft angle increases from 45° to 55°, the dissociation of nitrogen, ionization of nitric oxide and the degree of thermo non-equilibrium downstream of the second cone shock deepen. When aft angle beyond 55°, the degree of those thermochemical processes are not sensitive to aft angle. In the flows over 55° and 60° configuration, due to the expansion of the separation size, the dissociation reactions of molecule appear in the separation zone. In the separation zone and supersonic jet of 55° and 60° configuration, the vibrationally over-excited phenomenon occurs.

With the increase of the aft angle, the extension of the separation zone caused by the enhanced aft angle gradually weakens. The maximum wall heat flux and wall pressure gradually increase and move downstream. In addition, the increases of the aft angle induce more pressure and heat flux peaks, and cause larger heat and pressure oscillations in the separation zone and the supersonic jet. The larger aft angle increases the thermal load on the second cone, while the thermal load on the first cone decreases due to the expansion of the separation zone.

Overall, the significant differences of flow characteristics are between the flows of 50° and 55° configuration, causing by the transition of SSI type.

References

1. Dolling, D.S.: Fifty years of shock-wave/boundary-layer interaction research: What next? AIAA J. 39, 1517–1531 (2001).

2. Huang, W., Wu, H., Yang, Y., Yan, L., Li, S.: Recent advances in the shock wave/boundary layer interaction and its control in internal and external flows. Acta Astronaut. 174, 103–122 (2020).

3. Gaitonde, D.V.: Progress in shock wave/boundary layer interactions. Prog. Aerosp. Sci. 72 (2015).

4. Bertin, J.J., Cummings, R.M.: Fifty years of hypersonics: Where we've been, where we're going. Prog. Aerosp. Sci. 39, 511–536 (2003).

5. MacLean, M.G., Holden, M.S., Dufrene, M.: Comparison between CFD and measurements for real-gas effects on laminar shock wave boundary layer interaction I. AIAA paper. 2014-3366 (2014).

6. Swantek, A., Austin, J.: Heat Transfer on a Double Wedge Geometry in Hypervelocity Air and Nitrogen Flows. 50th AIAA Aerosp. Sci. Meet. New Horiz. Forum Aerosp. Expo. p. 284 (2012).

7. Olejniczak, J., Wright, M.J., Candler, J.V.: Numerical study of inviscid shock interactions on double-wedge geometries. J. Fluid Mech. 352, 1–25 (1997).

8. Holden, M.S., Wadhams, T.P., MacLean, M.G., et al.: Experimental Studies and Analysis to Investigate the Characteristics of Real Gas Air Flows in Regions of Shock Wave Boundary Layer Interaction Over a Blunted Double Cone Configuration. 22nd AIAA Int. Space Planes Hypersonics Syst. Technol. Conf., p. 5164 (2018).

9. Nompelis, I., Candler, G.: Numerical Investigation of Double-Cone Flow Experiments with High-Enthalpy Effects. 48th AIAA Aerosp. Sci. Meet. New Horiz. Forum Aerosp. Expo. p. 1283 (2010).

10. Holden, M.S.: Database of Aerothermal Measurements in Hypersonic Flow "Building Block" Experiments. 41st Aerosp. Sci. Meet. Exhib. p. 1137 (2003).

11. Holden, M.S., Wadhams, T.P., MacLean, M.G., Dufrene, A.T.: Measurements of Real Gas Effects on Regions of Laminar Shock Wave/Boundary Layer Interaction in Hypervelocity Flows for "Blind" Code Validation Studies. 21st AIAA Comput. Fluid Dyn. Conf. p. 2837 (2013).

12. Shoev, G.V., Bondar, Y.A.: Calculation of the heat flux and pressure on the double cone surface in a high-enthalpy non-equilibrium air flow. AIP Conf. Proc. (2019).

13. Shoev, G.V., Oblapenko, G., Kunova O., et al.: Validation of vibration-dissociation coupling models in hypersonic non-equilibrium separated flows. Acta Astronaut. 144, 147–159 (2018).

14. MacLean, M.G., Holden, M.S.: Validation and Comparison of WIND and DPLR Results for Hypersonic, Laminar Problems. 42nd AIAA Aerosp. Sci. Meet. Exhib. p. 529 (2004).

15. Expósito, D., Rana, Z.A.: Computational investigations into heat transfer over a double wedge in hypersonic flows. Aerosp. Sci. Technol. 92, 839–846 (2019).

16. Hao, J., Wang, J., Lee, C.: Numerical simulation of high-enthalpy double-cone flows, AIAA J. 55, 2471–2475 (2017).

17. Hao, J., Wen, C.Y.: Numerical investigation of oxygen thermochemical non-equilibrium on high-enthalpy double-cone flows. Int. J. Heat Mass Transf. 127, 892–902 (2018).

18. Kianvashrad, N., Knight, D.D.: Non-equilibrium effects on prediction of aerothermodynamic loading for a double cone. AIAA J. 57, 2946–2963 (2019).

19. Luo, S., Wu, L., Chang, Y., Li, X.: Thermochemical non-equilibrium and electromagnetic effects of double-cone in hypervelocity flow. Aerosp. Sci. Technol. 108041 (2022).

20. Ninni, D., Bonelli, F., Colonna, G., et al.: On the influence of non equilibrium in the free stream conditions of high enthalpy oxygen flows around a double-cone. Acta Astronaut. 201, 247–258 (2022).

21. Ninni, D., Bonelli, F., Colonna, G., et al.: Unsteady behavior and thermochemical non equilibrium effects in hypersonic double-wedge flows. Acta Astronaut. 191, 178–192 (2022).

22. Dai, C., Sun, B., Zhuo, C., et al.: Numerical study of high temperature non-equilibrium effects of double-wedge in hypervelocity flow. Aerosp. Sci. Technol. 124, 107526 (2022).

23. Durna, A.S., Ali Barada, M.E.H., Celik, B.: Shock interaction mechanisms on a double wedge at Mach 7. Phys. Fluids. 28 (2016).

24. Durna, A.S., Celik, B.: Time-periodic shock interaction mechanisms over double wedges at Mach 7. Shock Waves. 29, 381–399 (2019).

25. Vatansever, D., Celik, B.: Unsteady shock interaction mechanisms of high enthalpy reacting flows over double wedges at Mach 7. Phys. Fluids. 33 (2021).

26. Hao, J., Wen, C.Y.: Hypersonic flow over spherically blunted double cones. J. Fluid Mech. 896, A26 (2020).

27. Park, C.: Assessment of two-temperature kinetic model for ionizing air. J. Thermophys. Heat Transf. 3, 233–244 (1989).

28. Park, C.: Review of chemical-kinetic problems of future NASA missions, I: Earth entries. J. Thermophys. Heat Transf., 3, 385–398 (1993).

29. Anderson, J.D., Hypersonic and High Temperature Gas Dynamics. American Institute of Aeronautics and Astronautics, Reston, VA (2000).

30. Gupta, R.N., Yos, J. M., Thompson, R.A.: A Review of Reaction Rates and Thermodynamics and Transport Properties for an 11-Species Air Model for Chemical and Thermal Non-equilibrium Calculations to 30000 K. NASA Report. 1232 (1990).

31. Wilke, C.R.: A Viscosity Equation for Gas Mixtures, J. Chem. Phys. 18, 517–519 (1950).

32. Sutton, K., Gnoffo, P.: Multi-component diffusion with application to computational aerothermodynamics. 7th AIAAASME Jt. Thermophys. Heat Transf. Conf. p. 2575 (1998).

Dengke Li. First, Bo Sun. Second, Chunliang Dai.Third, Xiong Chen.Fourth

33. Batten, P., Clarke, N., Lambert, C., Causon, D.M.: On the Choice of Wavespeeds for the HLLC Riemann Solver. SIAM J. Sci. Comput. 18, 1553–1570 (1997).

34. Harten, A.: High resolution schemes for hyperbolic conservation laws. J. Comput. Phys. 49, 357–393 (1983).

35. Edney, B.: Anomalous heat transfer and pressure distributions on blunt bodies at hypersonic speeds in the presence of an impinging shock. Flygtekniska Forsoksanstalten, Stockholm (1968).

36. Babinsky, H., Harvey, J.K.: Shock Wave-Boundary-Layer Interactions. Cambridge University Press, Cambridge, New York (2011).

37. Passiatore, D., Sciacovelli, L., Cinnella, P., Pascazio, G.: Thermochemical non-equilibrium effects in turbulent hypersonic boundary layer., J. Fluid Mech. 941 (2022).

38. Tang, M.Z., Wang, G., Xie, Z.X., et al.: Aerothermodynamic characteristics of hypersonic curved compression ramp flows with bistable states. Phys. Fluids. 33 (2021).

39. Gai, S.L., Khraibut, A.: Hypersonic compression corner flow with large separated regions. J. Fluid Mech. 877, 471–494 (2019).